Geophysical Prospecting EAGE EUROPEAN ASSOCIATION OF GEOSCIENTISTS & ENGINEERS

Geophysical Prospecting, 2018, **66**, 857–871 doi: 10.1111/1365-2478.12623

Seismic attenuation, normal moveout stretch, and low-frequency shadows underlying bottom simulating reflector events

José M. Carcione[1,4], Ayman N. Qadrouh[2], Hervé Perroud[3], Davide Gei[1], Jing Ba[4]* and Stefano Picotti[1]

[1]*Istituto Nazionale di Oceanografia e di Geofisica Sperimentale (OGS), Borgo Grotta Gigante 42c, 34010 Sgonico, Trieste, Italy,* [2]*SAC—KACST, PO Box 6086, Riyadh 11442, Saudi Arabia,* [3]*Géosciences Montpellier–CNRS UMR 5243–Université de Montpellier, Place E. Bataillon, 34095 Montpellier, France, and* [4]*School of Earth Science and Engineering, Hohai University, Nanjing 211100, China*

Received July 2017, revision accepted January 2018

ABSTRACT

In many cases, the seismic response of bottom-simulating reflectors is characterised by low frequencies called "low-frequency shadow". Generally, this phenomenon is interpreted as attenuation due to partial saturation with free gas. Actually, this frequency loss may have multiple causes, with a normal moveout stretch as a possible candidate. To analyse this phenomenon, we compute synthetic seismograms by assuming a lossy bottom-simulating layer, with varying quality factor and thickness, bounded by the upper hydrate-brine/gas-brine and lower gas-brine/brine interfaces. First, we estimate the shift of the centroid frequency of the power spectrum as a function of the travelled distance of the seismic pulse. Then, we perform one-dimensional numerical experiments to quantify the loss of frequency of the seismic event below the bottom-simulating reflector as a function of the quality factor of the bottom-simulating layer and its thickness (due to wave interference). Then, we compute shot gathers to obtain the stacked section, with and without the normal moveout stretch correction and with and without the presence of wave attenuation in the bottom-simulating layer. The results indicate that the low-frequency shadow due to the normal moveout stretch is stronger than that due to attenuation and may constitute a false indicator of the presence of gas. In fact, often, the low-frequency shadow overlies events with higher frequencies, in contradiction with the physics of wave propagation. This is particularly evident when the low-frequency shadow is so extensive that the presence of high frequencies below cannot be justified by the acquisition geometry.

Key words: BSR, Attenuation, NMO stretch, low-frequency shadow.

1 INTRODUCTION

Bottom-simulating reflectors (BSRs) on seismic profiles are interpreted to represent the seismic signature of the base of gas-hydrate formations overlying a layer partially saturated with free gas. (Gas hydrates are clathrate compounds filling the sediment pores in which the host molecule is water and the guest molecule is typically methane.) Recently, Dewangan *et al.* (2014) analysed the effect of gas hydrate and free gas on seismic attenuation. The zones of gas hydrate, identified by the increase in seismic velocity, show high-quality factors (Q), a result that agrees with the rock physics models proposed by Carcione and Tinivella (2000), Gei and Carcione (2003), Carcione and Gei (2004) and Carcione *et al.* (2005a), and with the experimental results in Rossi *et al.* (2007). Similarly, Sain *et al.* (2009) found that the Q (256) estimated over the region with a strong BSR is found to be more than double the Q (100) derived for the region without any BSR or a weak

*E-mail: jba@hhu.edu.cn

BSR. These works indicate that the presence of free gas within the gas-hydrate stability zone increases seismic attenuation.

It is observed that the seismic response of the BSR is characterised by low frequencies, called the "low-frequency shadow" (LFS) by Taylor, Dillon and Pecher (2000). They state: "Low frequency shadows indicate high absorption in the overlying layers. Gas-charged layers cause high absorption in addition to a sharp drop in P-wave velocity.... We suggest that the shift to lower frequencies beneath the BSR is associated with free gas". In particular, in Geletti and Busetti (2011) (see Fig. 8), the seismic events below the BSR show remarkable low frequencies. Generally, the shift to low frequencies is interpreted as attenuation due to partial saturation with free gas (e.g., Vanneste *et al.* 2001).

These phenomena also appears in seismic exploration of hydrocarbons related to bright spots (Castagna, Sun and Siegfried 2003; Ebrom 2004; Wang *et al.* 2014). Del Ben *et al.* (2011) identified bright spots on the basis of low-frequency zones in the south Apulian foreland. However, some caution is required since the presence of low frequencies may be due to other causes, such as normal moveout (NMO) stretch, which is important at far offset traces (Dunkin and Levin 1973; Perroud and Tygel 2004). In fact, Castagna *et al.* (2003) state, "For every example shown, the shadow was stronger than the reservoir reflection at lower frequencies, suggesting that shadows are not necessarily a simple attenuation phenomenon because low-frequency energy must have been added or amplified by some physical or numerical process. Attenuation alone should simply attenuate higher frequencies, not boost lower frequencies". Actually, the LFS may have multiple causes, which are not mutually exclusive. Ebrom (2004) lists six stack-related causes, namely, NMO stretch, two due to attenuation, one due to wave interference, and another due to improper seismic deconvolution. Moreover, there is some controversy on this subject. According to Barnes (2013), only few examples of low-frequency shadows are convincing to reveal the presence of gas.

In this work, we focus our research on the effects caused by attenuation and NMO stretch, since the first is related to the so-called "direct hydrocarbon indicators", and the second seems to be the most important artefact introducing low frequencies (Ebrom 2004). The attenuation of the upper layers induces a shift of the spectrum centroid to low frequencies as the offset increases. In addition, attenuation in the BSR layer is very high due to mesoscopic-loss effects because of the presence of gas (e.g., Carcione and Picotti 2006), and this affects the reflection and transmission coefficients as a function of the incidence angle and offset. Moreover, the small thickness of the BSR layer implies interference effects, which affect the reflection coefficient and waveform. Finally, NMO stretch can cause a shift of the spectrum of the stacked reflection event to lower frequencies (Dunkin and Levin 1973), and therefore, stretch corrections are required to distinguish between physical attenuation and this artefact. The method used here to avoid the low frequencies due to NMO stretch is the algorithm proposed by Perroud and Tygel (2004). Canning and Malkin (2008) developed an un-stretch algorithm, which operates in the angle domain.

In order to study this phenomena, we compute 1D and 2D synthetic seismograms by assuming a high-loss BSR layer and varying the quality factor and thickness of the layer. First, we estimate the shift of the centroid frequency of the power spectrum as a function of the travelled distance. Then, we perform simple 1D experiments to quantify the frequency loss in seismic events below the BSR as function of the Q factor of the BSR layer and layer thickness (wave interference). Then, we compute shot gathers and perform the standard processing sequence to obtain the stacked section, with and without the NMO-stretch correction and with and without the presence of attenuation in the BSR layer. In all these cases, we evaluate the intensity of the LFS.

The media are described by a poroelastic model based on a generalisation of Gassmann equation. In particular, the upper medium containing gas hydrates and brine is a sediment whose skeleton has three phases, namely, quartz, clay, and gas hydrate, forming three frames. The model also describes the BSR layer partially saturated with gas as a particular case. The modelling algorithm is based on a spectrum of relaxation mechanisms, and the differential equations are solved in the space-time domain by using a direct method based on the Fourier pseudospectral method (e.g., Carcione 2014).

2 PETRO-ELASTICAL MODEL

Figure 1(a) shows the media (denoted by $j = 1,2,3$) and interfaces composing the system, where the bottom-simulating reflector (BSR) event is due to a composite reflection related to layer 2. The sediments above the BSR (medium 1) are saturated with brine containing clay and gas hydrate. This rock can be considered as a composite material with $n = 3$ frames, i.e., the rock frame (quartz), the clay frame, and that of the hydrate network. In the following, $i = 1$, 2, and 3 indicate the properties of quartz, clay, and gas hydrates, respectively. Carcione *et al.* (2005b) obtained the wet-rock (Gassmann) bulk modulus of a medium with n frames and

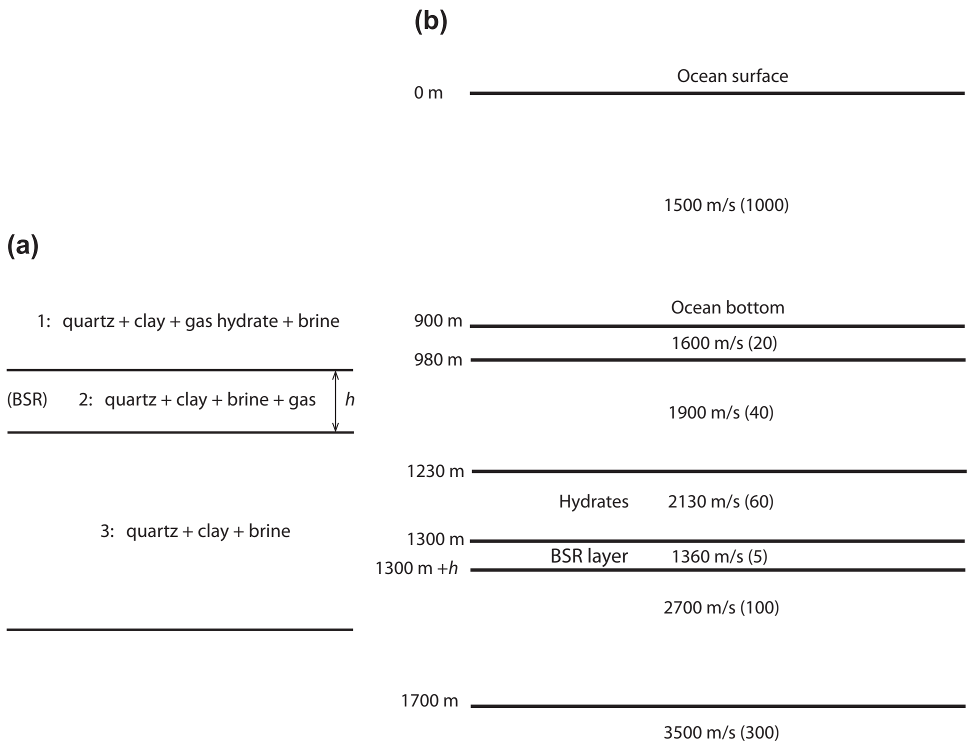

Figure 1 Geological model. Composition of the BSR system (a) and general model (b). The velocities and quality factors are indicated, the latter between parentheses.

one fluid. If ϕ_i is the fraction of the i-th solid and ϕ is the porosity, such that $\sum^n \phi_i + \phi = 1$, the Gassmann modulus is as follows:

$$K_G = \sum_{i=1}^{n} K_{mi} + \left(\sum_{i=1}^{n} \alpha_i\right)^2 M, \tag{1}$$

where

$$M = \left(\sum_{i=1}^{n} \frac{\phi_i'}{K_i} + \frac{\phi}{K_f}\right)^{-1}, \tag{2}$$

$$\phi_i' = \alpha_i - \beta_i \phi, \qquad \alpha_i = \beta_i - \frac{K_{mi}}{K_i}, \qquad \beta_i = \frac{\phi_i}{1-\phi}. \tag{3}$$

β_i is the fraction of solid i per unit volume of total solid. Here, $K_i, i = 1, \ldots n$, and K_f are the solid and fluid bulk moduli, respectively, and K_{mi}, $i = 1, \ldots n$ are the frame moduli.

A generalisation of Krief's model for a multi-mineral porous medium is used to obtain the frame moduli, as follows:

$$K_{mi} = (K_{\rm HS}/V)\beta_i K_i (1-\phi)^{A/(1-\phi)}, \qquad i = 1, \ldots, n, \tag{4}$$

(Carcione *et al.* 2005b), where A is a dimensionless parameter, $V = \sum_{i=1}^{n} \beta_i K_i$ is the Voigt average, and $K_{\rm HS} = (K_+ + K_-)/2$, where K_+ and K_- are the Hashin–Shtrikman (HS) upper and lower bounds (Mavko, Mukerji and Dvorkin 1998). The expression (4) is such that the composite modulus $K_m = \sum^n K_{mi}$ is consistent with the HS bounds when $\phi = 0$.

On the other hand, the dry-rock (and wet-rock) shear modulus of the composite is as follows:

$$\mu_m = \sum_{i=1}^{n} \frac{\mu_i}{K_i} K_{mi}, \tag{5}$$

where μ_i is the rigidity modulus of the ith solid.

Finally, the P-wave modulus is as follows:

$$E = K_G + \frac{4}{3}\mu_m. \tag{6}$$

The model is used to characterise all the media in Fig. 1 to obtain the elastic (lossless velocity) as follows:

$$c = \sqrt{\frac{E}{\rho}}, \tag{7}$$

where ρ is the composite density, given the following:

$$\rho = (1-\phi)\sum_{i=1}^{n} \beta_i \rho_i + \phi \rho_f, \tag{8}$$

where ρ_i and ρ_f are the densities of the i-th solid phase and fluid, respectively.

Medium 2 has brine and gas in the pores. When the fluids are not mixed in the pore volume, but distributed in patches, the effective bulk modulus of the fluid at high frequencies is higher than that predicted by Wood's model (White 1975; Mavko *et al.* 1998; Carcione and Picotti 2006). To obtain the bulk modulus of the gas–liquid mixture, we use an empirical law introduced by Brie *et al.* (1995). The effective bulk modulus is given as follows:

$$K_f = (K_b - K_g)S^e + K_g, \tag{9}$$

where K_b and K_g are the brine and gas bulk moduli, S is the brine saturation, and e is an empirical parameter. Equation (9) gives Voigt's mixing law for $e = 1$ and an approximation to Wood's model for $e = 40$. The fluid density in this medium is simply given by $\rho_f = S\rho_b + (1 - S)\rho_g$, where ρ_b and ρ_g are the brine and gas densities, respectively.

2.1 Anelastic characterisation of the layer

In this case, c becomes complex and frequency dependent in equation (7). In that equation, c corresponds to the high-frequency limit velocity and, E, to the unrelaxed modulus E_U. The phase velocity, attenuation factor, and quality factor of a viscoelastic medium are (e.g., Carcione 2014) as follows:

$$c_p = \left[\mathrm{Re}\left(\frac{1}{c}\right)\right]^{-1}, \qquad \alpha = -\omega \mathrm{Im}\left(\frac{1}{c}\right) \quad \text{and} \quad Q = \frac{\mathrm{Re}(c^2)}{\mathrm{Im}(c^2)}, \tag{10}$$

respectively, where, here, c denotes the complex velocity of the P-wave, ω is the angular frequency, $\omega = 2\pi f$, and "Re" and "Im" take real and imaginary parts.

We consider a constant quality factor, $\bar{Q}$, obtained with a spectrum of L Zener relaxation mechanisms, whose peak locations are equispaced in $\log \omega$ scale (see Section 2.4.6 by Carcione (2014)). We then have to find the relaxation times $\tau_{\epsilon l}$ and $\tau_{\sigma l}$ that give an almost constant Q in a given frequency band centred at $\omega_{0m} \equiv 1/\tau_{0m}$. This is the location of the mechanism situated at the middle of the band, which, for odd L, has the index $m = L/2 + 1$. The minimum quality factor of the L peaks is the same and is given as follows:

$$Q_0 = \frac{\bar{Q}}{L} \sum_{l=1}^{L} \frac{2\omega_{0m}\tau_{0l}}{1 + \omega_{0m}^2 \tau_{0l}^2}, \tag{11}$$

Table 1 Medium properties

Medium	ϕ_1	ϕ_2	ϕ_3	ϕ	c [m/s]	ρ [Kg/m^3]	$\bar{Q}$
1	0.34	0.22	0.04	0.4	2130	1937	60
2	0.34	0.22	0	0.44	1360	1906	5
3	0.6	0.05	0	0.35	2700	2086	100

where ω_{0m} is defined below and $\omega_{0l} \equiv 1/\tau_{0l}$ are the peak locations. Then, the relaxation times are as follows:

$$\tau_{\epsilon l} = \frac{\tau_{0l}}{Q_0}\left(\sqrt{Q_0^2 + 1} + 1\right) \quad \text{and} \quad \tau_{\sigma l} = \frac{\tau_{0l}}{Q_0}\left(\sqrt{Q_0^2 + 1} - 1\right). \tag{12}$$

If f_0 is the central frequency of the source wavelet, we assume that the centre peak is located at $\omega_{0m} = 2\pi f_0$.

Finally, the complex P-wave modulus is given as follows (Carcione 2014; equation (2.196)):

$$E(\omega) = E_U \left(\sum_{l=1}^{L} \frac{\tau_{\epsilon l}}{\tau_{\sigma l}}\right)^{-1} \sum_{l=1}^{L} \frac{1 + \mathrm{i}\omega\tau_{\epsilon l}}{1 + \mathrm{i}\omega\tau_{\sigma l}}, \tag{13}$$

where E_U is the unrelaxed, high-frequency limit modulus, obtained from the model introduced in the previous section (equation (7)). If $\omega \to \infty$, $E \to E_U$. Taking into account that $E = \rho c^2$, the quality factor is given by equation (10).

The cause of the high attenuation in the layer can be due to mesoscopic loss by wave-induced fluid flow (Müller, Gurevich and Lebedev 2010; Carcione 2014). It is assumed that the medium has patches of gas in a brine-saturated background. White's model (White 1975; Carcione and Picotti 2006) describes wave velocity and attenuation as a function of frequency, patch size, permeability, and viscosity. Attenuation and velocity dispersion are caused by fluid flow between patches of different pore pressures. The critical fluid diffusion relaxation scale is proportional to the square root of the ratio permeability to frequency. At seismic frequencies, the length scale is very large, and the pressure is nearly uniform throughout the medium, but as frequency increases, pore pressure differences can cause an important increase in P-wave velocity (Carcione and Picotti 2006).

3 MODELLING METHOD

The synthetic seismograms are computed with a modelling code based on the viscoacoustic stress–strain relation corresponding to the spectrum of relaxation mechanism introduced in the previous section. The equations are given in

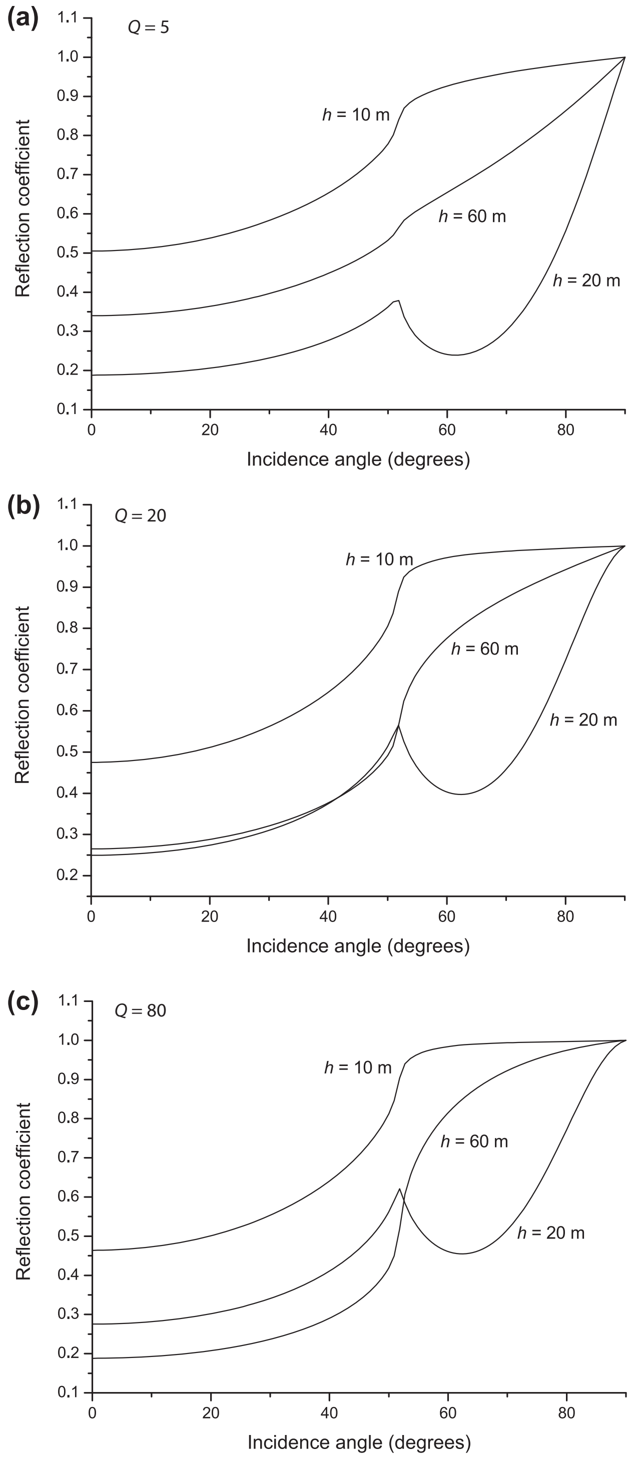

Figure 2 Real part of the reflection coefficient as a function of the incidence angle for different layer thicknesses and $Q = 5$ (a), $Q = 20$ (b), and $Q = 80$ (c). The source dominant frequency is $f_p = 25$ Hz.

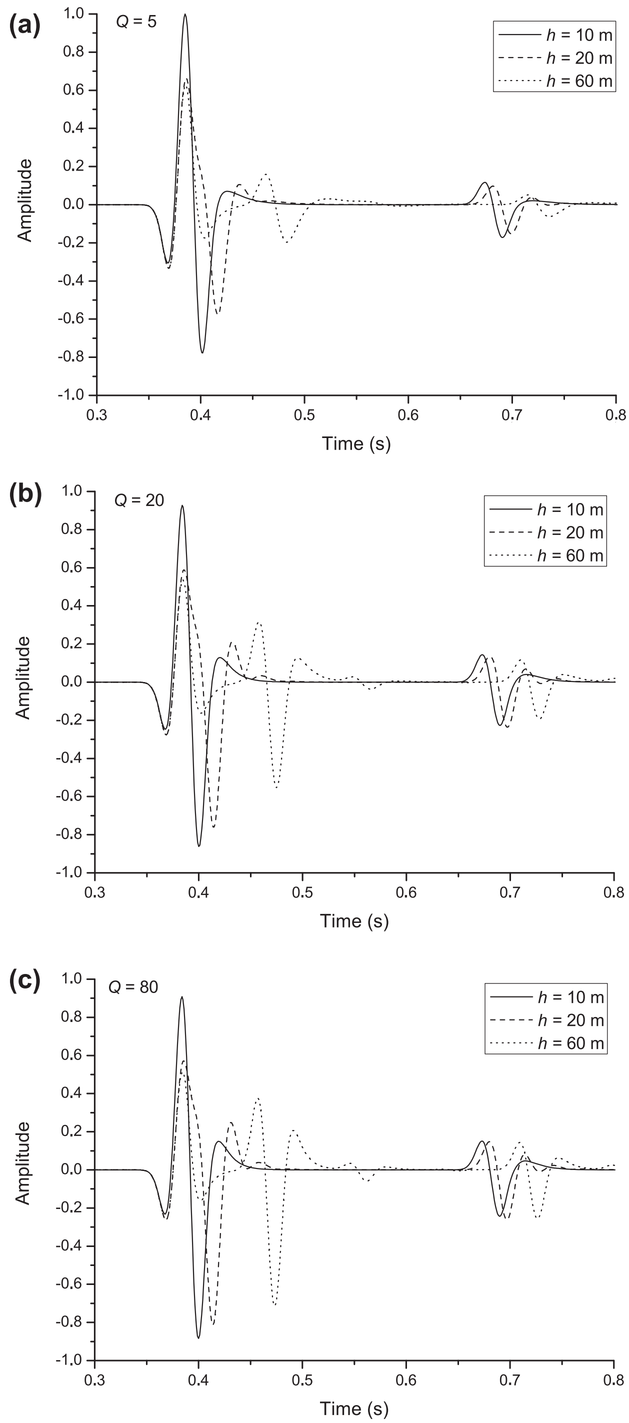

Figure 3 Comparisons between the normal-incidence seismic responses for different thicknesses of the BSR layer, where $Q = 5$ (a), $Q = 20$ (b), and $Q = 80$ (c). The source dominant frequency is $f_p = 25$ Hz.

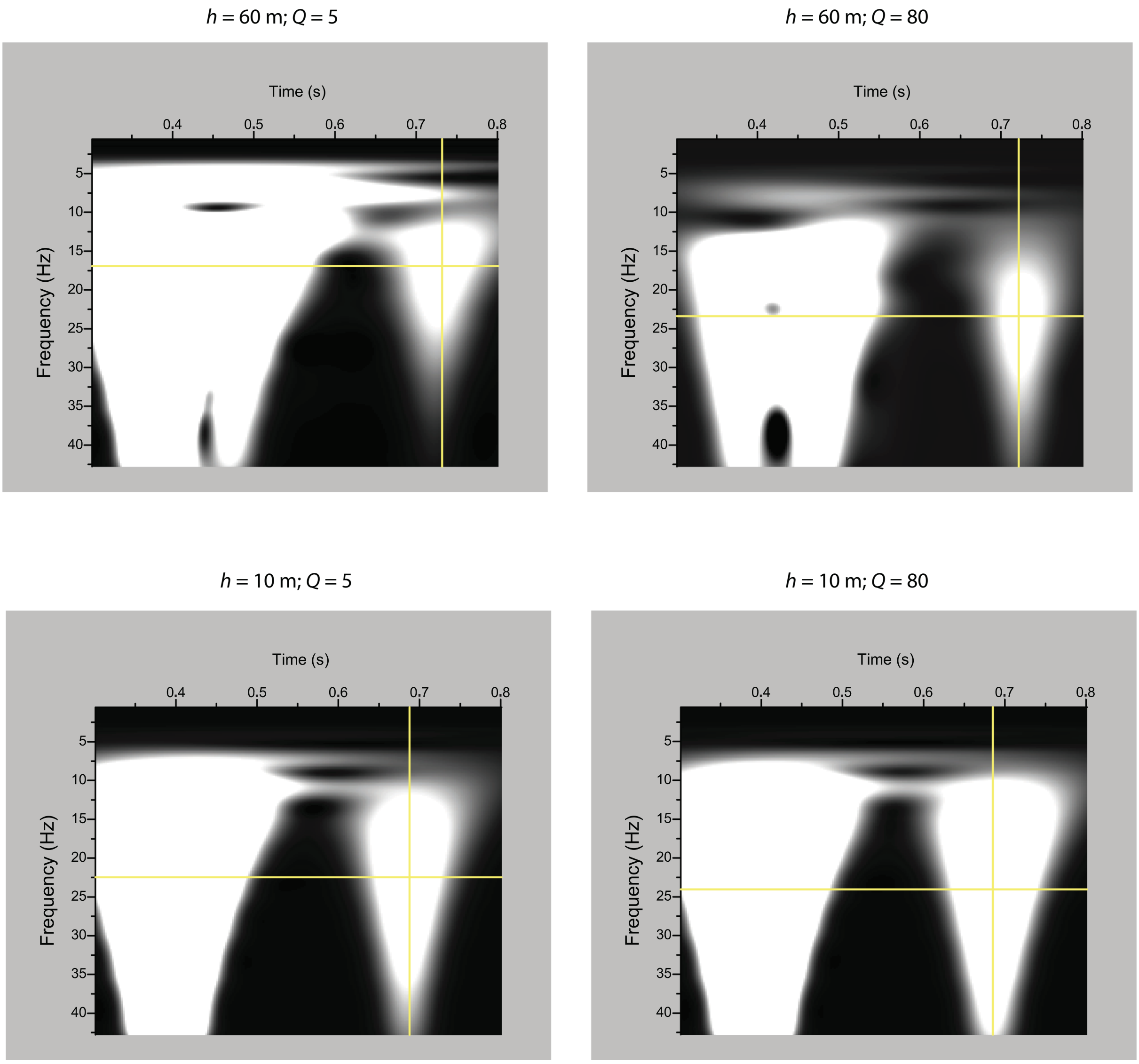

Figure 4 Spectrograms computed with the wavelet transform, where h denotes the thickness of the BSR layer and, Q, its quality factor.

Section 2.10.4 of Carcione (2014). The 2D particle velocity–stress formulation is as follows:

$$
\begin{aligned}
\dot{v}_x &= \frac{1}{\rho}\partial_x \sigma, \\
\dot{v}_z &= \frac{1}{\rho}\partial_z \sigma, \\
\dot{\sigma} &= E_U\left(\vartheta + \sum_{l=1}^{L} e_l\right) + s, \\
\dot{e}_l &= \varphi_l \vartheta - \frac{e_l}{\tau_{\sigma l}}, \qquad l = 1, \ldots, L, \\
\vartheta &= \partial_x v_x + \partial_z v_z
\end{aligned}
\tag{14}
$$

where v is particle velocity, σ is stress, s is the source (explosion), e_l are memory variables,

$$
\varphi_l = \frac{1}{\tau_{\sigma l}}\left(\sum_{l=1}^{L} \frac{\tau_{\epsilon l}}{\tau_{\sigma l}}\right)^{-1}\left(1 - \frac{\tau_{\epsilon l}}{\tau_{\sigma l}}\right), \tag{15}
$$

and a dot above a variable denotes time differentiation. The numerical algorithm is based on the Fourier pseudospectral method for computing the spatial derivatives and a 4th-order Runge–Kutta technique for calculating the wavefield recursively in time (e.g., Carcione 2014).

4 EXAMPLES

The medium properties are shown in Table 1, where the subindices along the first horizontal row denote quartz (1), clay (2) and gas hydrate (3), while the first column indicates the medium as given in Fig. 1(a). Values of the quality factor as low as 5 can be found in high-porosity unconsolidated sediments saturated with gas and can be explained with the mesoscopic attenuation theory (for more details about this loss model, see Carcione *et al.* 2012). Rossi *et al.* (2007, Fig. 10) report Q profiles with values of nearly 60 and 10 in the hydrate and bottom-simulating reflector (BSR) layers, respectively. The other properties are as follows: $K_1 = 35$ GPa, $K_2 = 20$ GPa, $K_3 = 8$ GPa, $K_b = 2.4$ GPa, $K_g = 0.007$ GPa, $\mu_1 = 35$ GPa, $\mu_2 = 10$ GPa, $\mu_3 = 3.3$ GPa, $\rho_1 = \rho_2 = 2.65$ g/cm^3, $\rho_3 = 0.92$ g/cm^3, $\rho_b = 1.04$ g/cm^3, $\rho_g = 0.07$ g/cm^3, $S = 91.6\%$ (the gas saturation is 8.4%), $A = 3$ and $e = 20.5$, where A is a typical value for the Krief equation (Carcione *et al.* 2005b) and the value of e is an average between the Voigt and Wood limits. The unrelaxed P-wave velocities are shown in Table 1, which agree with those of Fig. 9(c) in Geletti and Busetti (2011). The simulations consider the model shown in Fig. 1. We consider $L = 3$ relaxation mechanisms, with the centre peak located at the source dominant frequency f_p (see below), where the first peak is located at $f_p - 10$ Hz. (Three Zener kernels are enough to give a nearly-constant Q around the source central frequency.)

The 1D simulations have 495 grid points with a grid spacing of 5 m, whereas the 2D simulations have 693×561 grid points with 10 m spacing in the horizontal and vertical directions, respectively. The source $s = \delta(\mathbf{x})h(t)$ has the time history as follows:

$$h(t) = \left(u - \frac{1}{2}\right)\exp(-u), \qquad u = \left[\frac{\pi(t - t_s)}{T}\right]^2, \tag{16}$$

where T is the period of the wave and we take a delay $t_s = 1.4T$ to make the signal causal. The peak frequency is $f_p = 1/T$. The Runge–Kutta algorithm uses a time stepping of 0.5 ms and 1 ms in the 1D and 2D cases, respectively.

4.1 Reflection coefficients

Here, we compute the plane-wave reflection coefficients as a function of the Q factor and thickness of the BSR layer (e.g., Carcione 2014). Figure 2 shows the real part of the reflection coefficient of the BSR layer as a function of the incidence angle, for three layer thicknesses and three Q factors. First,

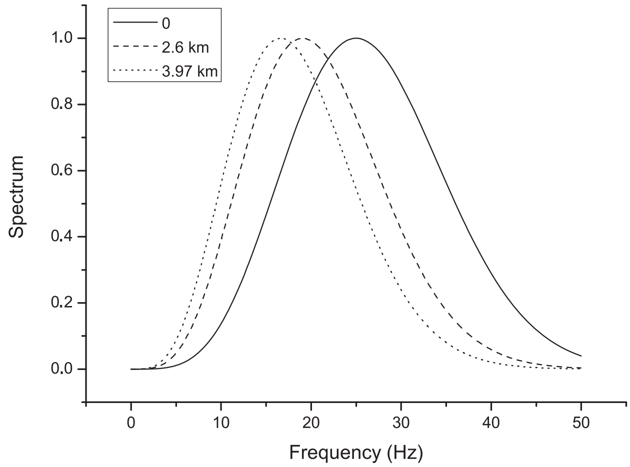

Figure 5 Spectra of the signal as a function of traveled distance for the reflection event corresponding to the BSR layer. Changes are due to the attenuation of the upper layers. The curves are normalised. The real maximum amplitudes with respect to the zero-offset case are 1 (0 km), 0.2 (2.6 km), and 0.07 (3.97 km).

the sign is always positive. Then, we observe significant differences as thickness change, although the trend is that the amplitude increases with angle. Note that at near offsets, the curves for $h = 20$ m and $h = 60$ m are hardly distinguishable for $Q = 20$. Hence, interference and Q may have similar effects. The results show that many of the effects can be counterintuitive, indicating that proper rock physics modelling is essential.

4.2 One-dimensional transient response: effects of Q

Next, we analyse the low-frequency shadow (LFS) below the BSR with a simple 1D model, i.e., the waveform and spectrum of the BSR event and those of the lower interface (see Fig. 1). Figure 3 shows 1D simulations for different Q values and thicknesses of the BSR layer, corresponding to the same values of Fig. 2. The source dominant frequency is 25 Hz. The BSR and lower-interface events can be observed at onset times of approximately 0.34 s and 0.65 s, respectively. The amplitude of the BSR event is maximum at $h = 10$ m, in agreement with Fig. 2. For $h = 10$ m, the BSR is one single event, whereas it is composed of two events for $h = 60$ m, because the events corresponding to the two interfaces composing the BSR system do not interfere. Attenuation affects the lower interface with minimum amplitudes for $Q = 5$. The importance of considering attenuation is evident, where the response of the lower interface of the BSR layer is highly attenuated (compare the dotted curves of Figs. 3(a) and (c). A

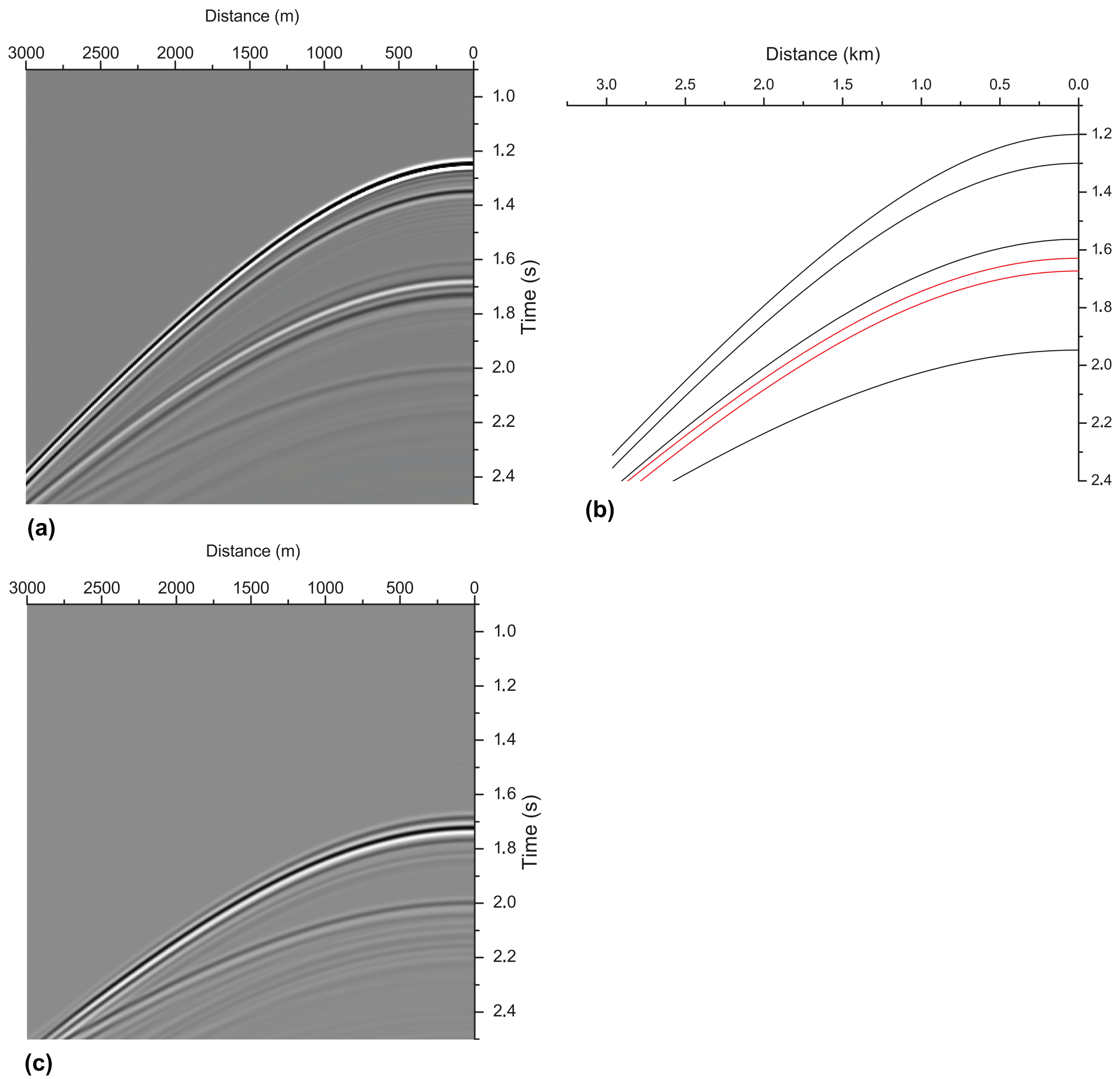

Figure 6 CMP gather for $Q = 5$ in the BSR layer (a), exact traveltimes (b), and difference between the seismograms computed with $Q = 5$ and $Q = 100$ in the BSR layer (c). The red curves correspond to the bottom and top of the layer, which has a thickness of 30 m.

spectrogram for the seismic trace can be computed by using the wavelet transform (Torrence and Compo 1998). Figure 4 shows spectrograms computed with the wavelet transform, where h denotes the thickness of the BSR layer and Q its quality factor. (The advantage of the wavelet transform over the Fourier transform is that the former is localised in both time and frequency, whereas the Fourier transform is only localised in frequency.) The vertical line indicates the location of the event reflected from the interface below the BSR layer, whereas the wider event, between 0.3s and 0.6 s, is the BSR response. The maximum frequency loss can be quantified as the shift of the centroid spectrum, approximately from 23 to 17 Hz, which occurs for the thicker layer, i.e., $h = 60$ m, due to the strong attenuation of the signal when traveling through the layer twice (downwards and upwards). The effect is not observable for a thickness of 10 m.

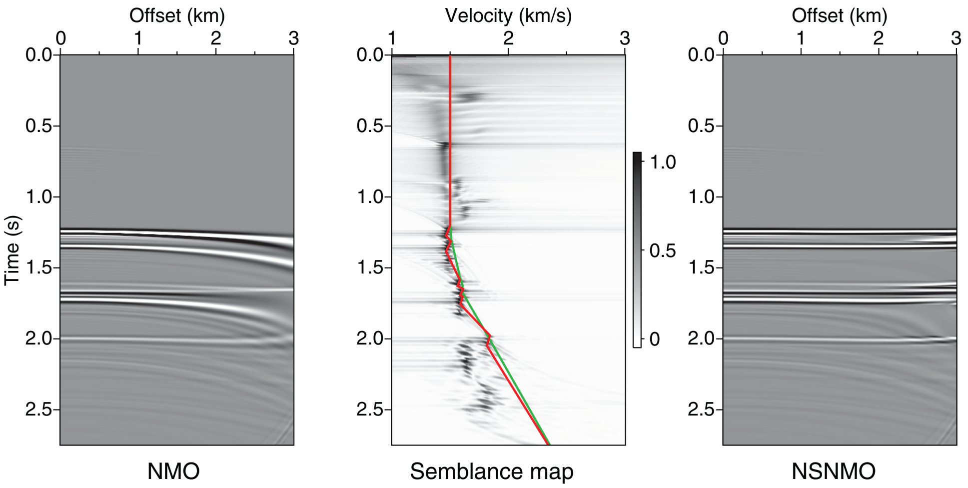

Figure 7 Synthetic CMP gather after conventional (left) and non-stretch (right) NMO corrections. The semblance map (middle) shows the time-velocity functions corresponding to the conventional (green curve) and non-stretch (red curve) cases.

4.3 Two-dimensional transient response: effects of Q and normal moveout stretch

Next, we analyse the effects due to the attenuation of the overburden. The average Q factor of a sequence of N layers of thickness h_i and quality factor Q_i is given in Appendix A, equation (A6). At normal incidence and down to the BSR layer, the average quality factor is $Q = 117$, with an average velocity $v = 1596$ m/s and a two-way propagation distance of 2.6 km at normal incidence. The values for the largest offset (3 km) are nearly similar but with an approximate travel distance of 3.97 km. The attenuation values (A4), quantifying the exponential decay, are 0.33 and 0.18, respectively at normal incidence at largest offset. In Appendix B, we show how the centroid f_c of the spectrum of a signal moves as a function of the traveled distance due to attenuation. Figure 5 shows the spectra of the signal as a function of traveled distance. The centroids are 26.4, 20.9, and 18.6 Hz at the source location, normal incidence, and largest offset, respectively. Hence, there is a frequency shift of approximately 8 Hz at the receiver located at 3 km from the source, due to the loss of high frequency by the attenuation of the upper layers.

A 2D common-midpoint (CMP) gather for a source-dominant frequency $f_p = 25$ Hz is displayed in Fig. 6(a), where the thickness of the BSR layer is 30 m. The events at 1.2 s and 2 s correspond to the reflection events of the ocean bottom and lower interface, respectively, whereas the red curves in Fig. 6(b) represent the exact traveltimes of the events reflected at the top and bottom of the BSR layer (Qadrouh *et al.* 2014) (arrival times correspond to the onset of the signals, not to the peak values). Fig. 6(c) shows the difference seismograms between that of Fig. 6(a) and one computed by considering $Q = 100$ in the BSR layer. The differences are substantial at normal incidence and largest offsets.

At large offsets, conventional normal moveout (NMO) yields significantly stretched events, affecting the frequency content of the data. To avoid this non-physical artifact, the non-stretch NMO method (NSNMO) proposed by Perroud

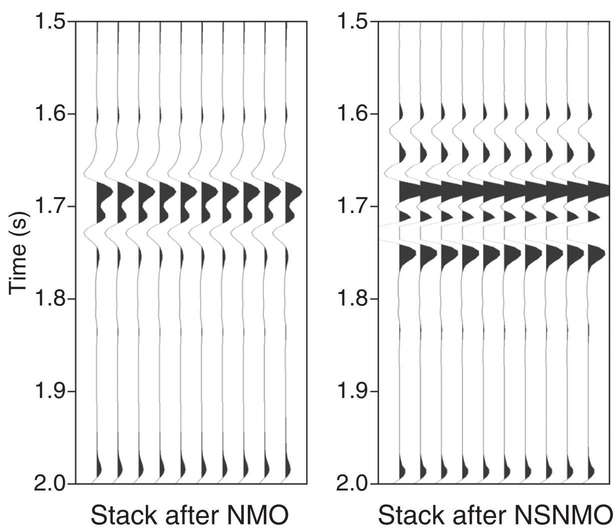

Figure 8 Stack traces in the BSR time range after conventional (left) and non-stretch (right) NMO corrections. The stack traces are repeated 10 times for a better visualisation.

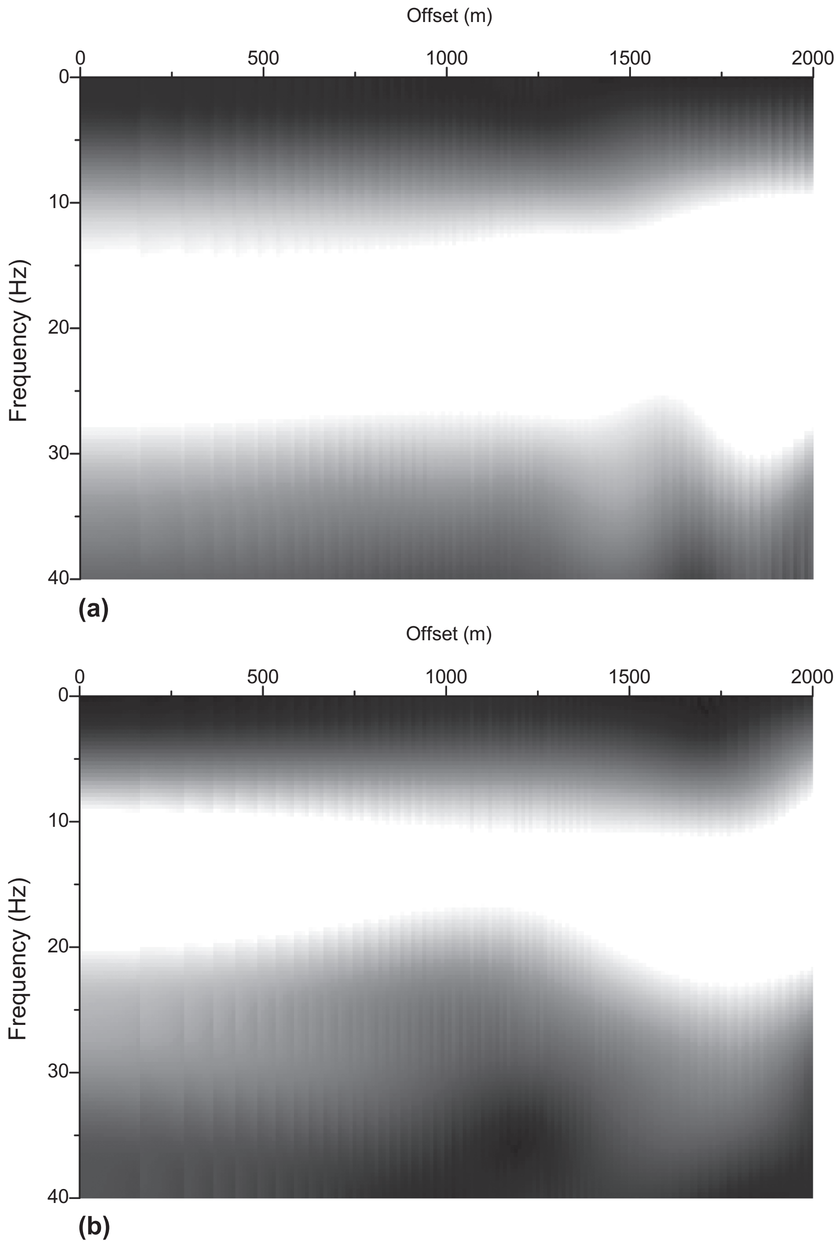

Figure 9 Spectrogram of the event below the BSR layer, corresponding to $Q = 100$ (a) and $Q = 5$ (b) in that layer. The thickness of the BSR layer is $h = 60$ m (1D case).

and Tygel (2004) is applied. The effects of the NMO stretch on the seismic signal versus offset are illustrated in Appendix C, where it is also shown how to correct the stretch and recover the high frequencies. Figure 7 (left) shows the NMO-corrected CMP gather with the conventional method, using a stretch limit large enough to avoid muting (samples with NMO stretch exceeding that limit are zeroed). The quality factor of the BSR layer is 100 in this example. The artificial low frequencies generated by the stretching can clearly be seen at large offsets, inducing to the false conclusion that the stacked event can be a physical LFS related to attenuation and the presence of gas. A semblance map is obtained for every sample, in a velocity range between 1 km/s and 3 km/s. A stretch limit of 30% has been applied, so the velocity analysis is conducted with limited aperture, in the validity range of the reflection-time hyperbolic approximation. According to the NSNMO method, the time-velocity function is adjusted to closely follow the shape of semblance peaks, with decreasing NMO velocity along the signal pulse for each event. The conventional (green curve) and non-stretch NMO

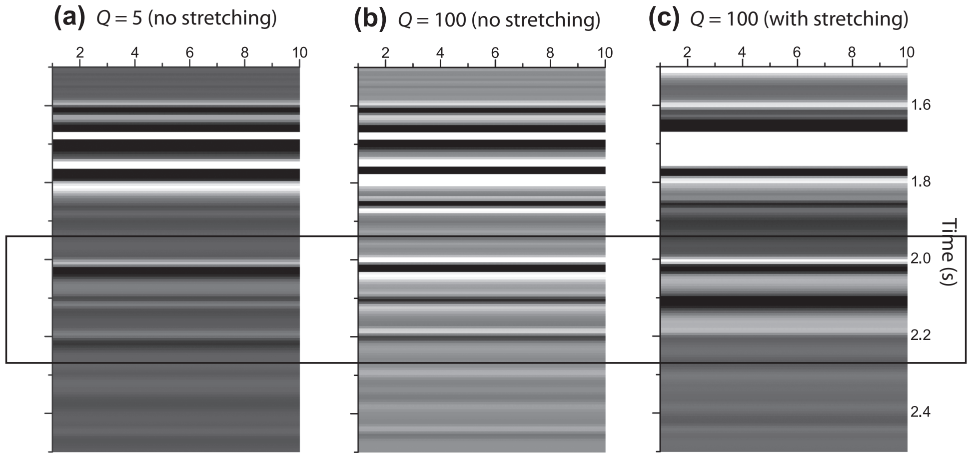

Figure 10 Stack with (c) and without NMO stretching (a and b). The quality factor of the BSR is reported. The box indicates the lower event, where the LFS should be present.

(red curve) time-velocity functions are shown in the middle panel of Fig. 7, overlying the semblance map. They closely match the semblance peaks corresponding to the primary P reflection events. The NSNMO correction is applied by using the adjusted time-velocity function (right panel in Fig. 7). The primary P events appear free of stretch and correctly flattened, so a stacked trace can be correctly obtained, without loss of frequencies. Residual NSNMO artefacts, although limited, can be seen at large offsets (right panel). They appear when events start to interfere with each other, as shown in Fig. 6(b) for the BSR layer reflections.

Figure 8 shows a stacked trace corresponding to the conventional and NSNMO corrections, using all offsets from 0 to 3 km (no stretch mute). Conventional NMO stretch muting was avoided in Fig. 7, so we could evaluate the effect of stretch on the stacked signal and its frequency spectrum. Such an effect would not appear if a severe stretch mute is applied in the course of processing, but then other undesirable effects would be produced with the loss of valuable information at large offsets (decrease of signal-to-noise ratio, loss of amplitude versus offset (AVO) analysis, etc.). With conventional NMO, the stretch effects are severe, so that close events largely interfere, as it is the case in the BSR time-range between 1.5 s and 2 s. On the other hand, with NSNMO, the events shape is preserved, and each interface can easily be identified. Moreover, the frequency content is preserved.

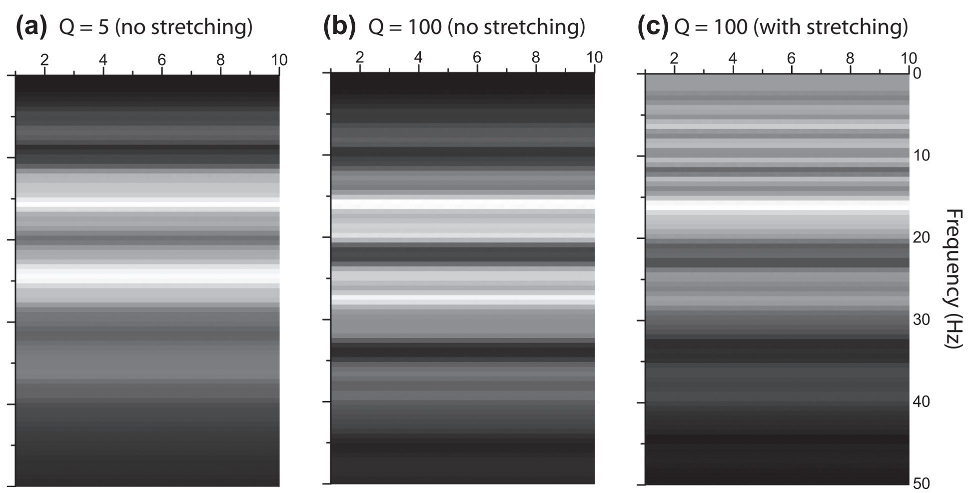

Figure 11 Frequency spectrum of the lower event indicated in Fig. 10, with (c) and without NMO stretching (a and b). The quality factor of the BSR is reported (2D case). Black and white correspond to low and high amplitudes.

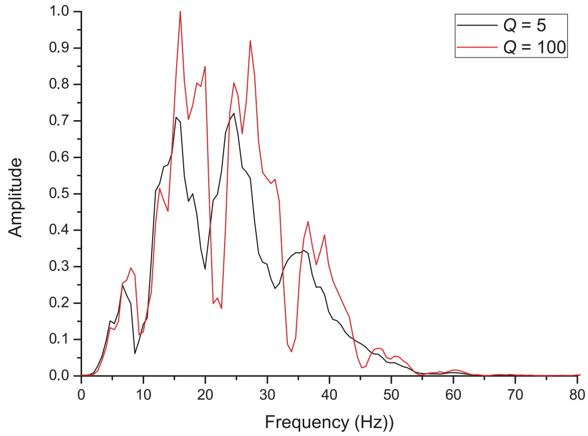

Figure 12 Frequency spectra of the lower event indicated in Fig. 10, without NMO stretching for Q = 5 and 100 in the BSR layer.

Next, we compute the spectrogram as a function of offset, in order to see the effect of attenuation on the reflection event corresponding to the interface below the BSR layer (at 1700 m). Figure 9 compares the results for $Q = 100$ (a) and $Q = 5$ (b) in the BSR layer. As expected, high-frequency components have been attenuated in the last case, with dominant frequencies around 15 Hz (a similar effect has been observed in the 1D case, see Fig. 4).

Finally, we obtain the stack and the frequency content of the lower event in the 2D case, for $Q = 5$ and $Q = 100$, with and without NMO stretching in the latter case. The results are shown in Figs. 10 and 11. A strong LFS can be observed in Fig. 10(c) between 2 s and 2.2 s due to the NMO stretching (event below the BSR). The stretching has also affected the upper event between 1.6 s and 1.8 s, where a strong smoothing and loss of frequency can be appreciated (see also Figs. 7(a) and 8 (left panel)). The loss of frequency can also be seen in Fig. 11(c). The effect of attenuation also removes high frequencies, but the effect is not so strong (see Figs. 10(a) and 11(a)). The centroid frequencies in Fig. 11 are 23 (a), 25 (b), and 20 Hz (c), respectively, indicating that stretching is a stronger high-cut filter than attenuation. Figure 12 compares the spectra without NMO stretching for low and high Q in the BSR layer, where we can observe the loss of frequencies in the first case.

5 CONCLUSIONS

We have analysed the seismic response of a bottom-simulating reflector (BSR) to identify the cause of the "low-frequency shadow" (LFS). The two most important causes are attenuation in the BSR layer (due to partial gas saturation) and NMO stretch. The main concern is the following: if frequency is lost due to attenuation, all the events below the BSR should have decreasing dominant frequencies as a function of depth, otherwise a single low-frequency event has to be due to NMO stretch or a similar artefact. First, a detailed analysis of the physics has been performed. The reflection coefficient of the BSR layer is always positive, and amplitude increases with angle in general. Moreover, wave interference and Q may have similar effects. Many of these can be counterintuitive, indicating that proper rock physics modelling is essential.

One-dimensional numerical seismograms and spectrograms show that attenuation affects the lower interface with minimum amplitudes for lower Q values, as expected. The maximum frequency loss can be quantified as the shift of the centroid spectrum. The gas-saturated layer has to be thick (compared with the wavelength) to observe a significant frequency and amplitude loss. The overburden may also have an effect, due to the loss of high frequencies by the attenuation of the upper layers. In the specific example, the centroid of the far-offset traces decreases by 8 Hz compared with the near-offset traces. The non-stretch NMO correction recover the resolution to identify the top and bottom of the BSR layer, and a stack section can be obtained without loss of frequencies.

A stack section obtained with significant NMO stretch can exhibit false LFS, which might be erroneously attributed to wave attenuation. The analysis shows that a physically consistent LFS for a BSR layer of 60 m and a quality factor of 5 (a lower limit) is not so strong as could be a the false LFS.

ACKNOWLEDGEMENTS

The authors wish to thank Yuriy Ivanov, Alexey Stovas, and two anonymous reviewers for useful and detailed comments.

REFERENCES

Barnes A.E. 2013. The myth of low-frequency shadows. *EAGE Workshop on Seismic Attenuation*.

Brie A., Pampuri F., Marsala A.F. and Meazza O. 1995. Shear sonic interpretation in gas-bearing sands. *SPE Annual Technical Conference*, **30595**, 701–710.

Canning A. and Malkin A. 2008. Removing NMO/migration stretch effects for improved AVO analysis. Proceedings of Hyderabad 2008.

Carcione J.M. 2014. *Wave Fields in Real Media. Theory and Numerical Simulation of Wave Propagation in Anisotropic, Anelastic, Porous and Electromagnetic Media*, 3rd edn, Elsevier.

Carcione J.M. and Gei D. 2004. Gas hydrate concentration estimated from P- and S-wave velocities at the Mallik 2L-38 research well, Mackenzie Delta, Canada. *Journal of Applied Geophysics* **56**, 73–78.

Carcione J.M., Gei D., Rossi G. and Madrussani G. 2005a. Estimation of gas hydrate concentration and free-gas saturation at the Norwegian-Svalbard continental margin. *Geophysical Prospecting* **53**, 803–810.

Carcione J.M., Gei D., Picotti S. and Michelini A. 2012. Cross-hole electromagnetic and seismic modeling for CO_2 detection and monitoring in a saline aquifer. *Journal of Petroleum Science and Engineering* **100**, 162–172.

Carcione J.M., Gei D. and Treitel S. 2010. The velocity of energy through a dissipative medium. *Geophysics* **75**, T37–T47.

Carcione J.M., Helle H.B., Santos J.E. and Ravazzoli C.L. 2005b. A constitutive equations and generalized Gassmann modulus for multi-mineral porous media. *Geophysics* **70**, N17–N26.

Carcione J.M. and Picotti S. 2006. P-wave seismic attenuation by slow-wave diffusion. Effects of inhomogeneous rock properties. *Geophysics* **71**, O1–O8.

Carcione J.M. and Tinivella U. 2000. Bottom simulating reflectors: seismic velocities and AVO effects. *Geophysics* **65**, 54–67. Errata: 2001, **66**, 984.

Castagna J.P., Sun S.J. and Siegfried R.W. 2003. Instantaneous spectral analysis: detection of low-frequency shadows associated with hydrocarbons. *The Leading Edge* **22**(2), 120–127.

Del Ben A., Forte E., Geletti R., Mocnik K. and Pipan M. 2011. Seismic exploration of a possible gas-reservoir in the south Apulia foreland. *Bolletino di Geofisica Teorica ed Applicata* **52**, 607–623.

Dewangan P., Mandal R., Jaiswal P., Ramprasad T. and Sriram G. 2014. Estimation of seismic attenuation of gas hydrate bearing sediments from multi-channel seismic data: a case study from Krishna-Godavari offshore basin. *Marine and Petroleum Geology* **58**, 356–367.

Dunkin J.W. and Levin F.K. 1973. Effects of normal moveout on a seismic pulse. *Geophysics* **38**, 635–642.

Ebrom D. 2004. The low-frequency gas shadow on seismic sections. *The Leading Edge* **23**(8), 772.

Gei D. and Carcione J.M. 2003. Acoustic properties of sediments saturated with gas hydrate, free gas and water. *Geophysical Prospecting* **51**(2), 141–158.

Geletti R. and Busetti M. 2011. A double bottom simulating reflector in the western Ross Sea (Antarctica). *Journal of Geophysical Research* **116**, B04101.

Mavko G., Mukerji T. and Dvorkin J. 1998. *The Rock Physics Handbook: Tools for Seismic Analysis in Porous Media*. Cambridge, UK: Cambridge University Press.

Müller T., Gurevich B. and Lebedev M. 2010. Seismic wave attenuation and dispersion resulting from wave-induced flow in porous rocks—A review. *Geophysics* **75**, A147–A164.

Perroud H. and Tygel M. 2004. Nonstretch NMO. *Geophysics* **69**, 599–607.

Qadrouh A.N., Carcione J.M., Botelho M.A.B., Harith Z.Z.T. and Salim A.M. 2014. On optimal NMO and generalised Dix equations for velocity determination and depth conversion. *Journal of Applied Geophysics* **101**, 136–141.

Rossi G., Gei D., Böhm G., Madrussani G. and Carcione J.M. 2007. Attenuation tomography: an application to gas-hydrate and free-gas detection. *Geophysical Prospecting* **55**, 655–669.

Sain K., Singh A.K., Thakur N.K. and Khanna R. 2009. Seismic quality factor observations for gas-hydrate-bearing sediments on the western margin of India. *Marine Geophysical Researches* **30**, 137–145.

Taylor M.H., Dillon W.P. and Pecher I.A. 2000. Trapping and migration of methane associated with the gas hydrate stability zone at the Blake Ridge Diapir: new insights from seismic data. *Marine Geology* **164**, 79–89.

Torrence C. and Compo G.P. 1998. A practical guide to wavelet analysis. *Bulletin of American Meteorological Society* **79**, 61–78.

Vanneste M., De Batist M., Golmshtok A., Kremlev A. and Versteeg W. 2001. Multi-frequency seismic study of gas hydrate-bearing sediments in Lake Baikal, Siberia. *Marine Geology* **172**, 1–21.

Wang L., Gao J., Xua Z., Weng B. and Jiang X. 2014. Hydrocarbon detection using adaptively selected spectrum attenuation. *Journal of Applied Geophysics* **105**, 59–66.

White J.E. 1975. Computed seismic speeds and attenuation in rocks with partial gas saturation. *Geophysics* **40**, 224–232.

Wyllie M.R.J., Gregory A.R. and Gardner L.W. 1956. Elastic wave velocities in heterogeneous and porous media. *Geophysics* **21**, 41–70.

APPENDIX A: TIME-AVERAGE EQUATION FOR THE QUALITY FACTOR

Wyllie, Gregory and Gardner (1956) obtained the so-called time average equation, which they applied to porous media. A similar version can be used to compute the average velocity of a stack of N layers (e.g., Carcione 2014) as follows:

$$v = \left(\frac{1}{h} \sum_{i=1}^{N} \frac{h_i}{v_i} \right)^{-1}, \qquad h = \sum_{i=1}^{N} h_i, \tag{A1}$$

where h_i is the thickness of the ith layer and v_i is its phase velocity.

Here, we obtain a similar equation to obtain an average quality factor of the stack of layers. We consider that the N layers have quality factors Q_i, $i = 1, \ldots, N$. A plane wave in a lossy medium attenuates as follows:

$$\prod_{i=1}^{N} \exp(-\alpha_i h_i) \approx \prod_{i=1}^{N} \exp\left(-\frac{\omega}{2 v_i Q_i} h_i \right), \tag{A2}$$

(e.g., Carcione 2014), where α_i is the attenuation factor. We may re-write equation (A2) as follows:

$$\exp\left(-\frac{\omega}{2} \sum_{i=1}^{N} \frac{h_i}{v_i Q_i} \right), \tag{A3}$$

or

$$\exp\left(-\frac{\omega h}{2vQ}\right), \tag{A4}$$

where

$$Q = \left(\frac{v}{h}\sum_{i=1}^{N}\frac{h_i}{v_i Q_i},\right)^{-1} \tag{A5}$$

is the average quality factor. Note that if we define the traveltime of each layer as $t_i = h_i/v_i$, the average or equivalent quality factor is as follows:

$$Q = \sum_{i=1}^{N} t_i \Bigg/ \sum_{i=1}^{N}\frac{t_i}{Q_i}\ , \tag{A6}$$

i.e., the weighted average of the single Q factors where the weights are the transit times.

APPENDIX B: CENTROID OF THE SIGNAL SPECTRUM

The 1D wavefield displacement in a viscoelastic medium is given, for instance, by Carcione, Gei and Treitel (2010) as follows:

$$U(\omega, x) = F(\omega)\exp(-\mathrm{i}kx), \tag{B1}$$

where k is the complex wavenumber. The power spectrum is as follows:

$$P(\omega) = |U(\omega)|^2 = |H|\exp(-2\alpha x), \tag{B2}$$

where H is the source spectrum

$$H(\omega) = \left(\frac{t_p}{\sqrt{\pi}}\right) o \exp(-o - \mathrm{i}\omega t_s), \qquad o = \left(\frac{\omega}{\omega_p}\right)^2,$$
$$\omega_p = 2\pi f_p, \tag{B3}$$

obtained as the Fourier transform of equation (16), and α is given by equation (10).

The centroid frequency of the power spectrum when the signal has traveled the distance x is as follows:

$$f_c(x) = \frac{\int_0^\infty \omega P(\omega, x)d\omega}{2\pi\int_0^\infty P(\omega, x)d\omega} = \frac{\int_0^\infty \omega|H|^2\exp(-2\alpha x)d\omega}{2\pi\int_0^\infty |H|^2\exp(-2\alpha x)d\omega}. \tag{B4}$$

APPENDIX C: CORRECTION OF THE NORMAL MOVEOUT STRETCH

Dunkin and Levin (1973) have explained the stretch effect after the NMO correction. Let us assume that, at a given offset, the signal before the NMO correction is $f(t)$. After the correction, the new (stretched) signal becomes $g(t) = f(t/a)$, where a is the stretch ratio, given below. The frequency domain version of this equation is $G(\omega) = aF(a\omega)$, where G and F are the Fourier transforms of f and g, respectively. The stretch ratio depends on the two-way traveltime, offset, and stacking velocity. The correction can be performed in the frequency domain by restoring each frequency component ω to the right value $a\omega$ and dividing the result by a, i.e., if G is the uncorrected spectrum, we have $F(\omega) = (1/a)G(\omega/a)$.

Here, we use the method of Perroud and Tygel (2004). Non-stretch NMO (NSNMO) is an implementation of the normal moveout (NMO) correction that is routinely applied to common-midpoint (CMP) reflections prior to stacking. The procedure avoids the undesirable stretch effects that are present in conventional NMO. Under NSNMO, a significant range of large offsets that normally would be muted in the case of conventional NMO can be used, thereby leading to better stack and velocity determinations, while preserving the frequency content. The basic processes, i.e., velocity analysis, NMO, and stack, are unchanged. An extra step is required to avoid the stretch effect, the adjustment of the time-velocity function obtained from the velocity analysis.

The theoretical basis is the following: when NMO is applied with a constant NMO velocity v_{NMO}, all the NMO hyperbolas converge to the same asymptote at large offsets, whose slope is $1/v_{\mathrm{NMO}}$. As they are not parallel, the amount of NMO time shift will vary along the pulse, generating the stretch. To avoid this, one has to keep the NMO hyperbolas parallel to each other. This cannot be strictly achieved within the whole offset range, but for a chosen offset, the distance between hyperbolas can be kept unchanged by adjusting the only free parameter, that is, v_{NMO}. In other words, for each sample that constitute the seismic pulse, a different v_{NMO} should be used to maintain the NMO hyperbolas separation.

If τ represents a time-shift since the onset of the seismic pulse, the following formula gives the adjusted NSNMO velocity $v(\tau)$ for an event at time $t(x)$ for offset x and NMO velocity v_{NMO} (obtained from the velocity analysis) at zero-offset time t_0 as follows:

$$v(\tau) = v_{\mathrm{NMO}}\left(1 + \frac{2}{1+\sqrt{1+\gamma^2}}\frac{\tau}{t_0}\right)^{-1/2}, \qquad \gamma = \frac{x}{t_0 v_{\mathrm{NMO}}}. \tag{C1}$$

One can observe that $v(\tau)$ decreases when τ increases, so the NSNMO-adjusted velocity always decreases along the seismic pulse. For relatively small τ, the decrease is quasi-linear and can therefore be described by a velocity at the beginning of the pulse and a velocity at the end of the pulse for the maximum τ whose value should correspond to the pulse length.

Strictly speaking, the adjusted velocity should be computed for each offset, so it should be different for every trace in the CMP gather. However, in practice, a significant stretch reduction can be obtained by using a single, averaged, adjusted time-velocity function in the full offset range. Furthermore, to simplify the process, this averaged time-velocity function can be obtained from the semblance map, by picking for each event both the top and the bottom of the corresponding semblance peak, whose shape normally displays the decreasing trend of velocity with time along the pulse length, if the semblance map has been computed with enough details. If available, an automatic semblance maxima picker should also follow this trend.